Journal of Biomechanics 93 (2019) 147–158

Contents lists available at ScienceDirect

Journal of Biomechanics

journal homepage: www.elsevier.com/locate/jbiomech
www.JBiomech.com

Magnetic resonance imaging based modeling of microvascular perfusion in patients with peripheral artery disease

Olga A. Gimnich [a,c], Jaykrishna Singh [b], Jean Bismuth [b], Dipan J. Shah [b], Gerd Brunner [a,b,c,*]

[a] Cardiovascular Imaging Research and Data Sciences Laboratory, Department of Medicine, Baylor College of Medicine, Houston, TX, USA
[b] Methodist DeBakey Heart and Vascular Center, Houston Methodist Hospital, Houston, TX, USA
[c] Penn State Heart and Vascular Institute, Pennsylvania State University College of Medicine, Hershey, PA, USA.

ARTICLE INFO

Article history:
Accepted 26 June 2019

Keywords:
Modeling
Computational fluid dynamics
Microvascular circulation
Magnetic resonance imaging
Peripheral artery disease

ABSTRACT

Peripheral artery disease (PAD) is associated with an increased risk of adverse cardiovascular events, impaired lower extremity blood flow and microvascular perfusion abnormalities in the calf muscles which can be determined with contrast-enhanced magnetic resonance imaging (CE-MRI). We developed a computational model of the microvascular perfusion in the calf muscles. We included 20 patients (10 PAD, 10 controls) and utilized the geometry, mean signal intensity and arterial input functions from CE-MRI calf muscle perfusion scans. The model included the microvascular pressure (p_v), outflow filtration coefficient (OFC), transfer rate constant (k^t), porosity (φ), and the interstitial permeability (K_{tissue}). Parameters were fitted and the simulations were compared across PAD patients and controls. Intra-observer reproducibility of the simulated mean signal intensities was excellent (intraclass correlation coefficients >0.995). k^t and K_{tissue} were higher in PAD patients compared with controls (4.72 interquartile range (IQR) 3.33, 5.56 vs. 2.47 IQR 2.10, 2.85; $p = 0.003$; and 3.68 IQR 3.18, 4.41 vs. 1.81 IQR 1.81, 1.81; $p < 0.001$). Conversely, porosity (φ) was lower in PAD patients compared with controls (0.52 IQR 0.49, 0.54 vs. 0.61 IQR 0.58, 0.64; $p = 0.016$). Porosity (φ) was correlated with the ankle brachial index ($r = 0.64$, $p = 0.011$). The proposed computational microvascular model is robust and reproducible, and essential model parameters differ significantly between PAD patients and controls.

1. Introduction

Peripheral artery disease (PAD) is a vascular disease represented by the formation of atherosclerotic lesions in the lower limbs (Fowkes et al., 2013, Gardner and Afaq, 2008, Lim, 2013, Brunner et al., 2013, Brunner et al., 2016, Kamran et al., 2016). PAD is associated with higher risk of coronary artery disease, myocardial infarction, and cardiovascular death (Gardner and Afaq, 2008, Newman et al., 1991). Approximately 27 million people suffer from PAD in Europe and North America (Criqui and Aboyans, 2015). PAD patients can experience leg pain, reduced exercise capacity, and the tissue loss. Improving small vessel blood flow at the level of the leg muscles is a challenge in PAD patients, however, tissue revascularization and therapeutic drugs that increase tissue perfusion show limited success (Silva et al., 2004, Stoner et al., 2008, Phelps and Garcia, 2009). Skeletal leg muscle perfusion using contrast-enhanced magnetic resonance imaging (CE-MRI) is of interest to study microvascular muscle perfusion in PAD patients (Brunner et al., 2016, Kramer, 2008, Thompson et al., 2005). Previous work (Brunner et al., 2016) suggests that muscle perfusion is heterogeneous across calf muscle compartments and reduced in PAD compared with controls. A computational model capable of measuring tissue transport properties based on CE-MRI perfusion data could be of clinical interest for assessing the severity of PAD and monitoring the response to novel drug treatment designed to enhance muscle perfusion and improve claudication pain.

Computational fluid dynamics (CFD) has good agreement with CE-MRI measurements in cardiovascular disease applications (Cibis et al., 2016, Singh et al., 2018, Hossain et al., 2015). Numerical models are an important tool to study tissue perfusion on different scales including from large vessels to the microcirculation (Debbaut et al., 2011, van der Plaats et al., 2004, Rani et al., 2006). The microvasculature can be modeled as a porous medium with permeability and porosity. Debbaut et al. developed a model of the blood flow in the human sinusoidal microcirculation using CFD methods. Blood was modeled as an incompressible and Newtonian fluid with a constant density and dynamic viscosity.

* Corresponding author at: One Baylor Plaza, Jewish Institute for Research, Room 506D, Houston, TX 77030, USA and 500 University Drive H047, Hershey, PA 17033, USA.
E-mail addresses: gbrunner@pennstatehealth.psu.edu, gbrunner@bcm.edu (G. Brunner).

https://doi.org/10.1016/j.jbiomech.2019.06.025
0021-9290/

This study presents the simulation of CE-MRI signal intensities in five distinct calf tissue regions including the anterior muscle (AM), lateral muscle (LM), deep posterior muscle (DM), soleus muscle (SM) and gastrocnemius muscle (GM). The aim of this work was to (i) estimate and model microvascular transport properties in the calf muscles, and (ii) compare the tissue transport properties between PAD patients and controls. The coupled equations of convection-diffusion and reaction terms were solved using Finite Element Methods (FEM). Simulated signal intensities were compared with CE-MRI signal intensities that permit the estimation of the best model parameters.

2. Materials and methods

PAD patients with life-style limiting intermittent claudication (IC) and controls were recruited at the Houston Methodist Hospital and the Michael E. DeBakey Veterans Affairs Medical Center (MEDVAMC), as described previously (Brunner et al., 2016, Holbrook et al., 2016). Matched controls and healthy controls without PAD were also recruited at the same sites. This study obtained approval from the local institutional review board (IRB) and all participants provided informed consent.

2.1. CE-MRI and image analysis

The acquired structural CE-MRI datasets were saved in DICOM format. The high-resolution saturation recovery gradient echo (GRE) pulse sequence had a slice thickness of 10 mm and a temporal resolution of 409 ms, as detailed previously (Brunner et al., 2016). We selected CE-MRI scans from 10 PAD patients, 5 matched controls and 5 healthy controls. Five distinct leg muscle domains (Fig. 1a, e) including the AM, LM, DM, SM, and GM were semi-automatically segmented using an in-house graphical user interface developed in MATLAB (MathWorks, 2012), as reported before (Brunner et al., 2016). The full model algorithm is available in Fig. 2.

2.2. Geometry reconstruction

For the 3D tissue computational domain, distinct leg muscle domains and leg contours (Fig. 1b, f) were imported in the ANSYS SpaceClaim application within the ANSYS Workbench (v. 18.2) software to create 3D volumes (Fig. 1c, g). Leg segments were modeled with a thickness of 10 mm to maintain continuity and clinical relevance (same as slice-thickness of CE-MRI perfusion scans).

2.3. Mathematical modeling

Tofts-Kermode two-compartment model

We based our computational microvascular model on the two-compartment Tofts-Kermode (TK) model (Tofts and Kermode, 1991) of plasma and tissue to describe the CE-MR signal enhancement with a gadolinium based contrast agent as a reaction term in the tissue regions

$$R_i = k^t\left(c_p - \frac{c_t}{\varphi}\right) \tag{1}$$

where c_p represents the concentration of the contrast agent in the blood; c_t is the concentration of the contrast agent in the tissue; k^t is the transfer rate constant for a given tissue; R_i is the reaction term in the i^{th} tissue region. φ is a computational approximation of the fraction of extracellular space or tissue porosity whereas $(1-\varphi)*100$ is an approximation of the percentage of fibrosis in the muscle domains in the computational model.

A convection-diffusion and reaction model was adopted to simulate 3D convection-enhanced delivery (CED) in the tissue regions. The tracer transport during CED was modeled using the convection-diffusion equation (Pishko et al., 2011, Pishko et al., 2012) as,

$$\frac{\partial c_t}{\partial t} + \frac{U_i}{\varphi}.\nabla c_t - D_i\nabla^2 c_t = k^t\left(c_p - \frac{c_t}{\varphi}\right) - OFC * p_i\frac{c_t}{\varphi} \tag{2}$$

where c_t is the concentration of contrast agent in the tissue; D_i is the diffusion of contrast agent; *OFC* is defined as the outflow filtration coefficient (OFC); and $p_i = 1066$ Pa is the interstitial fluid pressure (IFP) (Heldin et al., 2004). We utilized colloid osmotic pressures in the normal healthy capillaries as 8 mm Hg (1066.6 Pa) and therefore the IFP was set to $p_i = 1066$ Pa for the boundary condition on the cut ends of the leg surface (Heldin et al., 2004). This surface was not far away from the region of interest and hence a normal tissue pressure on the outlet surface was not utilized ($p_i = 0$ Pa). Pishko et al. (2011) defined IFP in the range of 0.86 – 1.4 KPa. The average value of the parameter (close to IFP of capillaries) allowed the estimation of the pressure in the region of interest.

Porous media model

The muscle tissue was modeled as a porous media (Pishko et al., 2011, 2012). The muscle domains were based on CE-MRI data of the user-defined model of elastic solid tissue with a porosity of

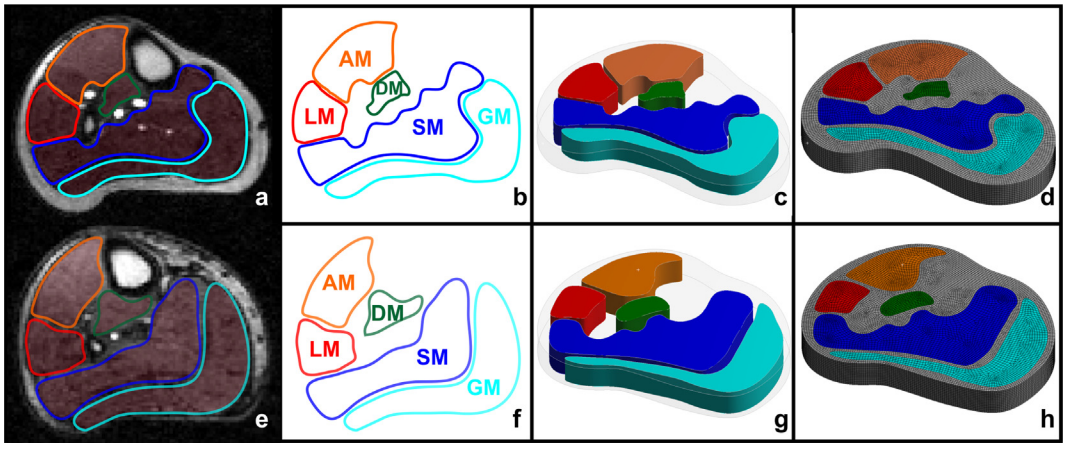

Fig. 1. (a, e) CE-MR images of a control and PAD patient; (b, f) for semi-automatically segmented leg muscle regions of a control and a PAD patient; (c, g) 3D models a control and a PAD patient; and (d, h) meshed domains of AM: anterior muscle, LM: lateral muscle, DM: deep posterior muscle, SM: soleus muscle, and GM: gastrocnemius muscle.

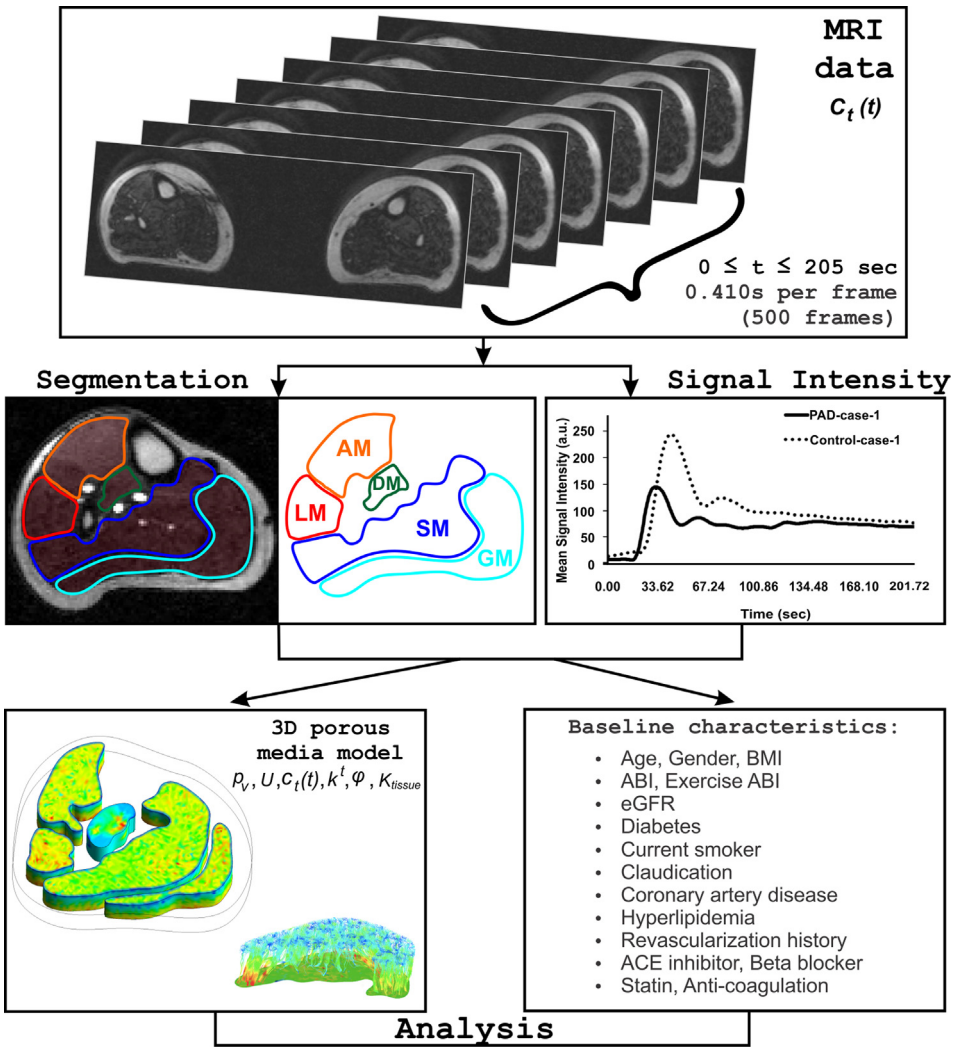

Fig. 2. Algorithm depicting the various steps involved in the computational microvascular model, including MRI data acquisition, segmentation, arterial input function (AIF) of a healthy control (dotted line) and a PAD patient (solid line) described in terms of mean signal intensity, model, and analysis.

20–80% (Table 1). In tissues, the continuity equation and Darcy's law were used to solve the interstitial fluid pressure IFP (p_i) and tissue averaged interstitial fluid velocity IFV (U_i) as,

$$\nabla . U_i = \frac{k^t}{k^{avg}} K_{tissue} \frac{S_A}{V} (p_v - p_i - \sigma(\pi_v - \pi_i)) - OFC * p_i \tag{3}$$

$$U_i = -\frac{K_{tissue}}{\mu} \left(\frac{\varphi}{1-\varphi} \right) \nabla p_i \tag{4}$$

k^{avg} is the average value of k^t;the second term on the right of equation (3). $K_{tissue} \frac{S_A}{V}$ is the capillary filtration coefficient (CFC), where, K_{tissue} is the tissue permeability; $\frac{S_A}{V}$ is the microvascular surface area per unit volume; p_v is the microvascular pressure (MVP); p_i is the IFP, σ is the average osmotic reflection for plasma protein, π_v is the osmotic pressure of plasma in the microvasculature, and π_i is the osmotic pressure in the interstitial space; the parameter K_{tissue} represents the interstitial permeability to fluid flow and is reflective of the composition of the extracellular matrix (Pishko et al., 2011). Next, K_{tissue}/μ was scaled by porosity which describes heterogeneity or porosity dependent hydraulic conductivity in the muscle tissue in the computational model. The ratio $\left(\frac{\varphi}{1-\varphi}\right)$ in equation (4) describes an approximation of the degree of flow versus non-flow (fibrosis). The ratio $\frac{k^t}{k^{avg}}$ in equation (3) accounts for plasma leakiness heterogeneities in the muscle tissue (Pishko et al., 2011); $(p_v - p_i)$ is the difference between the MVP and IFP; μ is the blood viscosity. More details on the porous media model are listed in Appendix A (*Porous Media Model*).

The transient value of the flow properties such as blood perfusion velocity and pressure were determined in each muscle domain. Blood perfusion was assumed to be transient, incompressible flow. Mass sources were used for introducing additional fluid into the simulation. The amount of fluid introduced was specified as fluid mass flux (on boundaries).

The arterial input function obtained from the CE-MRI scans (Brunner et al., 2016) specific to each muscle group were applied for the simulation (Fig. 2) and corresponded to the mean signal intensity of the contrast agent in the blood plasma. The full information about the model parameters is available in Table 1. We have modeled changes in signal intensities based on the administration of a gadolinium-based contrast agent rather than actual blood flow velocities. Signal intensities for the boundary conditions

Table 1
Fixed and fitted parameters of the simulations.

Parameters	Variable	Tissue	Type	Bounds\Value	References
π_v	Osmotic pressure in microvasculature	Calf Muscle	Fixed	2670 Pa or 20 mmHg	(Pishko et al., 2011)
π_i	Osmotic pressure in tissue	Calf Muscle	Fixed	200 Pa	(Debbaut et al., 2012, Brunner et al., 2016, Pishko et al., 2011)
p_i	Interstitial fluid pressure	Calf Muscle	Fixed	1066 Pa	(Heldin et al., 2004)
σ	Average osmotic reflection coefficient	Calf Muscle	Fixed	0.82	(Rippe et al., 1985)
μ	Blood viscosity	Blood	Fixed	$3.5 \cdot 10^{-3}$ Pa s	(Leong et al., 2013)
D_i	Self-diffusion coefficient of contrast agent	Calf Muscle	Fixed	$1.83 \cdot 10^{-9}$ m^2/s	(Dietrich et al., 2010)
ρ	Density	Calf Muscle	Fixed	1060 kg/m^3	(Bouillard et al., 2011, Davidson et al., 2014, Johnston et al., 2006)
Y	Elasticity Module	Calf Muscle	Fixed	0.4 MPa	(Frauziols et al., 2013, Grishina et al., 2016)
T	Temperature	Calf Muscle/ Blood	Fixed	37 °C	(Dubuis et al., 2012, Kenner, 1989)
ζ	Resistance of blood	Calf Muscle	Fixed	$2.5 \cdot 10^9$ $mmHg/m^3$	(Siggers et al., 2014)
p_v	Microvascular pressure	Calf Muscle	Free	6666.7 Pa (or 50 mmHg)* 50–170 mmHg	Estimated from curve fitting and literature (Stylianopoulos and Jain, 2013, Thompson et al., 2005, Yang et al., 2013)
CFC	Capillary filtration coefficient	Calf Muscle	Free	$7.216 \cdot 10^{-6}$ (1/Pa s)* $1 \cdot 10^{-7}$ (1/Pa s)	Estimated from curve fitting and literature (Pishko et al., 2011)
OFC	Outflow filtration coefficient	Calf Muscle	Free	$6 \cdot 10^{-7}$ to $15 \cdot 10^{-7}$ (1/Pa s)*	Estimated from curve fitting
k^t	Transfer rate constant	Calf Muscle	Free	$0.6 \cdot 10^{-3}$ to $1 \cdot 10^{-2}$* 1/s $4 \cdot 10^{-2}$ 1/s	Estimated from curve fitting and literature (Ren et al., 2015)
φ	Porosity	Calf Muscle	Free	0–1* 0.12	Estimated from curve fitting and literature (Smye et al., 2007)
K_{tissue}	Interstitial permeability to fluid flow	Calf Muscle	Free	$1.27 \cdot 10^{-9}$ to $2.98 \cdot 10^{-5}$ m^2 * $1.56 \cdot 10^{-9}$ to $3.64 \cdot 10^{-14}$ m^2	Estimated from curve fitting and literature (Debbaut et al., 2012)

* Estimated from curve fitting.

were obtained from CE-MRI scans of PAD patients and controls. However, the equations remain expressed in velocities rather than in changes of arbitrary signal intensities from CE-MRI scans.

2.3.1. Mathematical modeling with a non-newtonian fluid

Several studies have previously reported on the use of a Newtonian fluid approximation for similar types of models (Javadzadegan et al., 2019, Vankan et al., 1998, Bouillot et al., 2015, Zhao et al., 2018, Bonfiglio et al., 2010, Boyd et al., 2007, Zhang et al., 2015). However, we have also performed the same models with a non-Newtonian fluid for 10 out of the 20 cases (5 PAD patients and 5 controls) in order to compare with the Newtonian fluid approach. The dynamic viscosity of human blood in dependency of the shear rate was set up as variations of shear rates from 0.1 s^{-1} to 1000 s^{-1} at a constant temperature of 37 °C. We used the Carreau-Yasuda model as done in Boyd et al. (2007), which is a more generalized Carreau model. Then, blood was modeled as a non-Newtonian fluid using Carreau-Yasuda model to determine blood viscosity, as described by Zhang et al. (2015). The relationship between shear rate and viscosity was expressed as

$\eta\dot{\gamma} = \eta + (\eta_0 - \eta_\infty)\left[1 + (\lambda\dot{\gamma})^2\right]^{(n-1)/2}$ where η_∞ and η_0 are the infinite and zero shear rate viscosities, and λ is the relaxation time constant. The model has been found to fit to the experimental data with the following parameters: $\eta_\infty = 3.45 \cdot 10^3$ kg/m · s, $\eta_0 = 5.6 \cdot 10^{-2}$ kg/m · s, $n = 0.3568$ and $\lambda = 3.313$ s.

2.4. Mesh

For the computational domain, each segmented 3D muscle region of the controls and PAD patients was meshed using Ansys Mesh (Fig. 1d, h). The cell size of each muscle region was setup based on the grid mesh and the transient time step sensitivity tests.

2.4.1. Grid test

The grid independence test was performed to assess mesh quality by varying the number of control volumes in the computational domain. A final element mesh was selected to resolve the velocity vectors and capture the hemodynamics at various regions in different muscle groups.

The leg geometry was discretized into three different mesh categories: hexahedral mesh, tetrahedral mesh with and without boundary layer (hybrid mesh) using ANSYS Workbench (v.18.2). The modelling results were evaluated in three different planes taken in the AM, LM, DM, SM and GM separately with fixed porous materials parameters and boundary conditions. The variation of less than 5% was observed for maximum simulated signal intensity, and average pressure for grid size ranging from 200,000 to 250,000 elements. Therefore, the optimum size of 237,917 tetrahedral elements consisting of 13 layers by model thickness was used.

Tetrahedral hybrid mesh and hexahedral elements showed close agreement with the simulated signal intensity and pressure variation unlike the tetrahedral mesh toward as higher mesh size in the range of 150,000–180,000 elements. The variation was less than 0.7% between the tetrahedral hybrid and hexahedral mesh while in the tetrahedral mesh it was greater than 3%. Hence, a hexahedral mesh in the range of 85,000–100,000 elements per muscle volume was used over tetrahedral mesh for further evaluation purposes due to similar variation and fewer complications in the grid generation.

The global mesh size was set to 0.001 m. To ensure an accurate analysis of the muscles, a finer mesh was applied to the muscle sites (0.0008 m for AM, LM, SM, 0.0005 m for DM, GM). Model sizes ranging from 57,000 to 95,000 hexahedral elements consisting of 13 layers by model thickness were used with the unstructured mesh.

2.4.2. Transient time step sensitivity test

A time step sensitivity test was done to select the appropriate time step for the transient analysis. CE-MRI was measured on aver-

age over 205 s and the optimum time step was obtained through time step sensitivity test during transient analysis. The FEM (CFX ANSYS v.18.2) of the control group was used to perform the sensitivity test. The transient analysis was performed with 0.051 s (4000 steps), 0.103 s (2000 steps), 0.410 s (500 steps) and 1.025 s (200 steps). A common plane taken at mid-section of the FEM was used to analyze the maximum simulated signal intensity and average pressure for different time steps.

2.5. Curve fitting and error analysis

The resulting solution was integrated over the muscle tissue domain to get the mean signal intensity as a function of time. Mean square error (*MSE*) and mean absolute percentage error (*MAPE*) were calculated as a measure of estimating the best agreement between simulated and CE-MRI signal intensities. The *MSE* was computed as,

$$MSE = \frac{1}{n}\sum_{t=1}^{n}\left(\hat{y}_t - y_t\right)^2 * 100\%$$

where $\hat{y}_i$ represents the vector of predicted values and y_i represents the experimental values; and n is the number of time steps. *MAPE* was computed as,

$$MAPE = \frac{1}{n}\sum_{t=1}^{n}\left|\frac{y_t - \hat{y}_t}{y_t}\right| * 100\%$$

2.6. Model analysis

For model robustness, we analyzed the AM of a PAD patient (Fig. 1e) with the parameter values in Table 1 which were selected from the literature (Bouillard et al., 2011, Brunner et al., 2016, Dubuis et al., 2012, Frauziols et al., 2013, Grishina et al., 2016, Hinghofer-Szalkay and Greenleaf, 1987, Johnston et al., 2006, Kenner, 1989, Leong et al., 2013, Stylianopoulos and Jain, 2013, Thompson et al., 2005, Yang et al., 2013). We have varied each parameter by decreasing and increasing them over a range from 50% to 200%, respectively. Variation of the diffusion coefficient (D_i) of the contrast agent did not influence the mean signal intensity over time. A similar observation has been reported previously by Pishko et al. (2011). Variations in the interstitial permeability to fluid flow (K_{tissue}) in the muscle tissue, osmotic pressures (π_v, π_i) and osmotic reflection coefficient (σ) did not influence the mean signal intensity over time.

2.7. Statistical analysis

Variables were expressed as median (interquartile range [IQR]), percentages or frequencies. The nonparametric Mann-Whitney test was used to assess the difference between unpaired group data. Categorical group data were analyzed with the Chi-square or Fisher's exact test. The strength of correlations was described as weak ($r < 0.3$), medium ($0.3 \leq r < 0.5$), or strong ($r \geq 0.5$) (Cohen, 1988). Reproducibility analyses were performed using intra-class correlation coefficients (ICC) with a 2-way random-effects model (Shrout and Fleiss, 1979). The agreement of the reproducibility analysis is considered poor for an ICC < 0.30, moderate-to-good for an ICC of 0.30–0.70, and excellent for an ICC > 0.70 (Shrout and Fleiss, 1979, Carod-Artal et al., 2009).

All analyses were performed using StatalC 13. Statistical significance is indicated as $*$ ($p < 0.05$), $**$ ($p < 0.01$), and $***$ ($p < 0.001$).

3. Results

3.1. Baseline characteristics

A total of 20 individuals (10 PAD patients, 5 matched-controls, 5 healthy controls) were included in this study. There was no difference in age, gender, body mass index (BMI), and estimated glomerular filtration rate (eGFR) between PAD patients and matched controls (Table 2). PAD patients had a lower ankle brachial index (ABI) and were more likely diabetic and hypertensive compared with controls.

3.2. Computational microvascular model

Electronic Supplementary Material Fig. 1 shows the simulated and experimental mean signal intensities of a control (Electronic Supplementary Material Fig. 1a) and PAD (Electronic Supplementary Material Fig. 1b) patient for muscle domains AM, LM, DM, SM, and GM, respectively. We have varied the microvascular pressure (p_v), CFC, OFC and porosity over a range of −50% to 200%. The mean signal intensity profile was sensitive to MVP (Fig. 3a), OFC (Fig. 3c) and tissue porosity (Fig. 3d). The CFC was sensitive in the order of magnitude from the optimal value (Fig. 3b). *MSE* and *MAPE* for training the models were less than 5% (Fig. 3). Electronic Supplementary Material Table 1 shows the parameter values for PAD and control cases.

3.3. Computational microvascular model reproducibility

Intra-rater reproducibility for simulated mean signal intensity of a PAD patient over all time steps was excellent for the AM (intra-class correlation [ICC]: 0.999 confidence interval [CI]: 0.978, 1.0) and similar for the other muscle groups (Table 3a). Transient time step sensitivity test showed that the maximum simulated signal intensity and average pressure during 500 and 2000 time steps were almost identical (less than 0.02%) without any considerable difference with quite less at 4000 time step (less than 0.07%); however, there was a difference for 125 time steps (more than 6%). Inter-rater reproducibility for simulated mean signal intensity of 3 PAD patients and 5 controls over all time steps was excellent for the AM (PAD: 0.984 CI: 0.982, 0.985; Controls: 0.988 CI: 0.987, 0.989) and of a similar agreement for the LM, DM, SM, and GM, respectively (Table 3b, c).

3.4. Computational microvascular model: comparison between a Newtonian and Non-Newtonian fluid

Reproducibility analysis for simulated mean signal intensity of 5 PAD patients over all time steps was excellent between Newtonian and Non-Newtonian models (Fig. 4) for the AM (intra-class correlation [ICC]: 0.945 confidence interval [CI]: 0.941, 0.950), LM ([ICC]: 0.993, [CI]: 0.992, 0.993), DM ([ICC]: 0.969, [CI]: 0.967, 0.972), SM ([ICC]: 0.963, [CI]: 0.960, 0.966), and GM ([ICC]: 0.992, [CI]: 0.992, 0.993) (Table 4a).

Reproducibility analysis for simulated mean signal intensity of 5 controls over all time steps was excellent for the DM ([ICC]: 0.880, [CI]: 0.871, 0.888), AM ([ICC]: 0.987, [CI]: 0.986, 0.988), LM ([ICC]: 0.993, [CI]: 0.992, 0.993), SM ([ICC]: 0.992, [CI]: 0.991, 0.993), and GM ([ICC]: 0.980, [CI]: 0.978, 0.982) (Table 4b).

3.5. Computational microvascular model parameters

The simulated signal intensity of the contrast agent is shown in Fig. 5 at different time points (seconds). Averaged over all muscle groups, k^t and K_{tissue} were higher in PAD patients compared with

Table 2
Baseline characteristics.

Variable	PAD (n = 10)	Matched controls (n = 5)	P-value (PAD vs Matched Controls)	Healthy controls (n = 5)	P-value (Matched Controls vs Healthy Controls)
Age (years)	67.6 (7.6)	65.6 (7.1)	0.63	34.6 (4.8)	0.001
Gender male, no (%)	6 (60)	4 (80)	0.44	5 (100)	0.29
BMI (kg/m^2)	30.0 (6.4)	26.9 (5.2)	0.36	27.1 (4.0)	0.94
ABI	0.7 (0.4)	1.3 (0.1)	0.003	N/A	N/A
Exercise ABI	0.6 (0.4)	1.3 (0.1)	0.006	N/A	N/A
eGFR (mL/min/1.73 m^2)	79.3 (24.0)	81.3 (12.4)	0.86	N/A	N/A
Diabetes, no (%)	6 (60)	0 (0)	0.025	0 (0)	–
Hypertension, no (%)	9 (90)	2 (40)	0.039	0 (0)	0.11
Current smoker, no (%)	3 (30)	0 (0)	0.20	0 (0)	–
Claudication, no (%)	8 (80)	0 (0)	0.003	0 (0)	–
Coronary artery disease, no (%)	6 (60)	1 (20)	0.14	0 (0)	0.29
Hyperlipidemia, no (%)	8 (80)	2 (40)	0.12	0 (0)	0.11
Revascularization history, no (%)	4 (40)	0 (0)	0.099	0 (0)	–
ACE inhibitor, no (%)	3 (30)	0 (0)	0.17	0 (0)	–
Beta blocker, no (%)	3 (30)	0 (0)	0.17	0 (0)	–
Statin, no (%)	7 (70)	2 (40)	0.54	0 (0)	0.11
Anti-coagulation, no (%)	3 (30)	1 (20)	0.49	0 (0)	0.29

Values are reported as mean (standard deviation) or as number (percentage). N/A not applicable (not measured).
ABIs are listed for the more symptomatic side. Exercise ABI (n = 7).
ABI: Ankle brachial index, ACE: angiotensin-converting enzyme, BMI: body mass index, eGFR: estimated glomerular filtration rate.

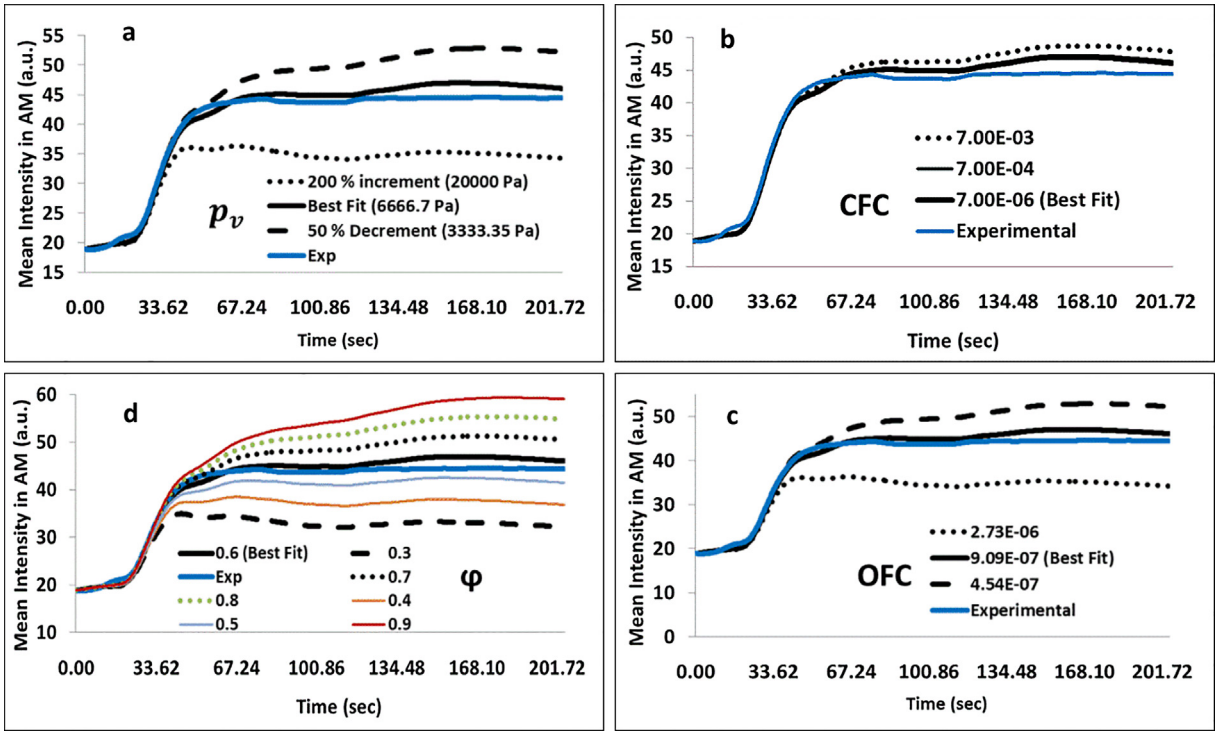

Fig. 3. Representative plot of the mean signal intensity with respect to change in (a) microvascular pressure (p_v) (b) the capillary filtration coefficient (CFC) (c) the outflow filtration coefficient (OFC) and, (d) the fraction of extracellular space (φ). The solid lines represent the optimal parameter (best fit) whereas dashed lines represent a decrease of 50% and the dotted lines represent an increase by 200% except in (d), whereas the mean signal intensity was simulated for a range of ±8.33%.

controls (4.72 IQR: 3.33, 5.56 vs. 2.47 IQR 2.10, 2.85; p = 0.003; and 3.68 IQR 3.18, 4.41 vs. 1.81 IQR 1.81, 1.81; p < 0.001, Table 5). Conversely, porosity (φ) averaged over all muscle groups was lower in PAD patients compared with controls (0.52 IQR 0.49, 0.54 vs. 0.61 IQR 0.58, 0.64; p = 0.016) (Electronic Supplementary Material Fig. 2). Modeling parameters were heterogeneous across individual calf muscle groups (Electronic Supplementary Material Table 2). In PAD patients, compared to controls, K_{tissue} was significantly higher in all five muscle groups, whereas k^t was significantly increased in the AM, DM, and SM but not in the LM and GM (Fig. 6). Similarly, p_v was significantly higher in the DM (p = 0.003) for PAD patients as compared to controls but was not different for the other muscles. Porosity (φ) was significantly lower in PAD patients compared with controls in the SM and GM but higher for the DM. There was no group difference for the OFC.

3.6. Correlation of model parameters with patient characteristics

The ABI was significantly correlated with φ when averaged over controls and PAD patients ($r = 0.64$, $p = 0.011$). k^t was significantly correlated with the ABI for controls ($r = 0.94$, $p = 0.017$) but not

Table 3
Intra-observer (a) and inter-reader variability of simulated mean signal intensity of a PAD patient (b) and a control (c) for each muscle region (AM, LM, DM, SM, GM) determined by intra-class correlation (ICC) coefficient using a two-way model.

(a)

	Intra-observer ICC for AM	Intra-observer ICC for LM	Intra-observer ICC for DM	Intra-observer ICC for SM	Intra-observer ICC for GM
Individual ICC	0.999	0.998	0.998	0.995	0.999
(95% CI)	0.978–1	0.966–0.999	0.964–0.999	0.922–0.999	0.995–1
Average ICC	1	0.999	0.999	0.998	1
(95% CI)	0.993–1	0.989–1	0.988–1	0.972–1	0.998–1

ICC was calculated for each time step, 1 PAD patient (number of targets 500) and for 3 independent calculations with different mesh size in range 0.0005–0.0008 m.

(b)

	Inter-observer ICC for AM	Inter-observer ICC for LM	Inter-observer ICC for DM	Inter-observer ICC for SM	Inter-observer ICC for GM
Individual ICC	0.984	0.978	0.855	0.881	0.98
(95% CI)	0.982–0.985	0.976–0.979	0.844–0.865	0.872–0.89	0.979–0.982
Average ICC	0.992	0.989	0.922	0.937	0.99
(95% CI)	0.991–0.992	0.988–0.99	0.915–0.928	0.932–0.942	0.989–0.991

ICC was calculated for each time step, 5 cases (number of targets 2479) and for 2 independent raters.

(c)

	Inter-observer ICC for AM	Inter-observer ICC for LM	Inter-observer ICC for DM	Inter-observer ICC for SM	Inter-observer ICC for GM
Individual ICC	0.988	0.972	0.915	0.873	0.927
(95% CI)	0.987–0.989	0.969–0.975	0.907–0.923	0.86–0.884	0.92–0.934
Average ICC	0.994	0.986	0.956	0.932	0.962
(95% CI)	0.993–0.995	0.984–0.987	0.951–0.96	0.925–0.939	0.958–0.966

ICC was calculated for each time step, 3 cases (number of targets 1498) and for 2 independent raters.
ICC: intra-class correlation; CI: confidence interval.

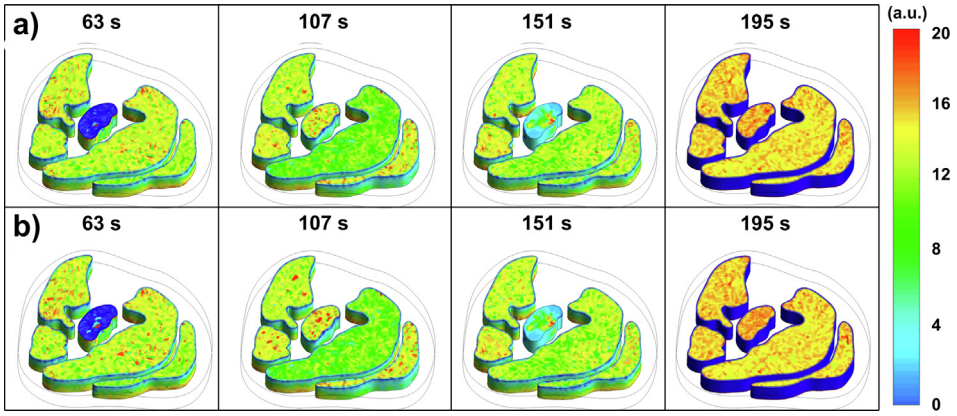

Fig. 4. Simulated signal intensities of contrast-enhanced MRI calf muscle perfusion (AM, LM, DM, SM, GM) for a PAD patient at different time points (seconds): (a) Newtonian model, (b) Non-Newtonian model.

Table 4
Reproducibility analysis of the simulated mean signal intensity of controls and PAD patients for each muscle region (AM, LM, DM, SM, GM), as determined by intra-class correlation (ICC) using a two-way model for non-Newtonian and Newtonian models.

(a) PAD Patients (n = 5)

	Inter-observer ICC for AM	Inter-observer ICC for LM	Inter-observer ICC for DM	Inter-observer ICC for SM	Inter-observer ICC for GM
Individual ICC	0.945	0.993	0.969	0.963	0.992
(95% CI)	0.941–0.950	0.992–0.993	0.967–0.972	0.960–0.966	0.992–0.993
Average ICC	0.972	0.996	0.984	0.981	0.996
(95% CI)	0.970–0.974	0.996–0.997	0.983–0.986	0.980–0.983	0.996–0.996

ICC: intra-class correlation; CI: confidence interval. ICC was calculated for each time step, 5 cases (Number of targets 2479) and for 2 observations.

(b) Controls (n=5)

	Inter-observer ICC for AM	Inter-observer ICC for LM	Inter-observer ICC for DM	Inter-observer ICC for SM	Inter-observer ICC for GM
Individual ICC	0.987	0.993	0.880	0.992	0.980
(95% CI)	0.986–0.988	0.992–0.993	0.871–0.888	0.991–0.993	0.978–0.982
Average ICC	0.994	0.996	0.936	0.996	0.990
(95% CI)	0.993–0.994	0.996–0.997	0.931–0.941	0.996–0.996	0.989–0.991

ICC: intra-class correlation; CI: confidence interval. ICC was calculated for each time step, 5 cases (Number of targets 2498) and for 2 observations.

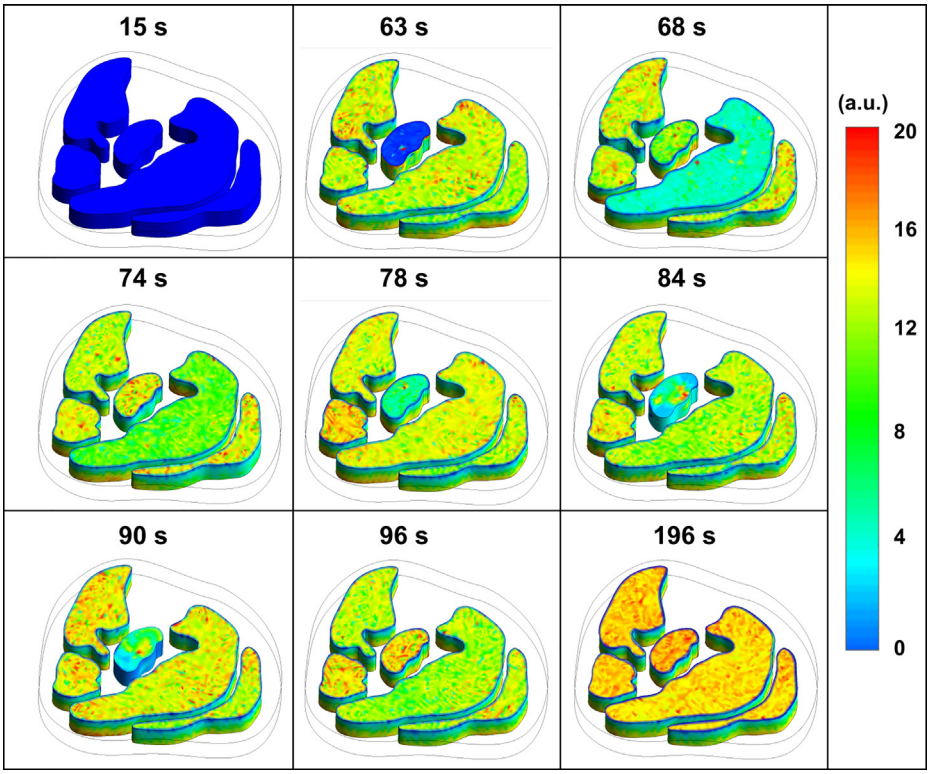

Fig. 5. Simulated signal intensities of contrast-enhanced MRI calf muscle perfusion (AM, LM, DM, SM, GM) for a PAD patient at different time points (seconds).

Table 5
Analyse of baseline patient characteristics and modeling parameters.

Variable	Control	PAD	Total	P-Value
k^t	2.47 (2.10, 2.85)	4.72 (3.33, 5.56)	3.59 (2.39, 4.74)	0.003
K_{tissue}	1.81 (1.81, 1.81)	3.68 (3.18, 4.41)	2.75 (1.81, 3.49)	0.001
φ	0.61 (0.58, 0.64)	0.52 (0.49, 0.54)	0.5663 (0.508, 0.63)	0.016
OFC	15.03 (11.96, 18.02)	13.17 (9.07, 12.46)	14.1 (9.79, 17.49)	0.08
$\boldsymbol{p}_v$	48.59 (47.76, 50.31)	52.02 (49.48, 56.48)	50.31 (47.85, 53.51)	0.06

All values are medians and interquartile range (IQR). P-values were calculated with the Kruskal-Wallis rank test. Control group: n = 10; PAD group: n = 10.

for PAD patients ($r = -0.05$, $p = 0.88$). k^t was inversely correlated with hypertension ($r = -0.89$, $p = 0.042$) among controls but not for PAD patients ($r = -0.1$, $p = 0.79$). There was a trend for a positive correlation of K_{tissue} with age when averaged over controls and PAD patients ($r = 0.41$, $p = 0.07$) and with the ABI among controls ($r = 0.86$, $p = 0.06$). All other correlations were not significant (Table 6).

4. Discussion

This study presents the simulation of CE-MRI signal intensity in five distinct calf muscle regions including the anterior, lateral, deep posterior, soleus and gastrocnemius muscles. This work (i) estimated and modelled transport properties in the calf muscles and (ii) compared tissue transport properties between PAD patients and controls. In this study $k^t$was significantly higher in PAD patients compared to controls when analyzed over five calf muscles regions and across distinct muscle domains. The transfer rate could be higher in tissues with damaged cells and could have a higher accumulation of contrast agent due to ruptured cell membranes allowing the contrast agent to diffuse into the extracellular compartments (Maestrini et al., 2014). Tissue permeability was significantly higher in PAD patients compared to controls when analyzed over all muscles regions and across distinct muscle domains. On the other hand, the fraction of extracellular space (φ) was significantly lower in PAD patients compared to controls. Our results indicate that the fraction of extracellular space (φ) was heterogeneous across muscle groups for DM, SM and GM which could be due to differences in muscle fiber composition across leg muscles and an increase in connective tissue. Wu et al. (2008) reported similar findings in a study of 24 controls indicating that heterogeneity of calf muscle perfusion could be attributed to differences in muscle fiber composition across leg compartments.

The differences in muscle fiber types may explain the differences of $k^t$and K_{tissue} across muscle groups, as PAD is associated with muscle atrophy, a complex process that results in denervation and a decrease in type II (glycolytic) muscle fiber area (Regensteiner et al., 1993). Robbins et al. (2011) found an association of leg muscle capillary density and peak hyperemic blood flow in patients with lower extremity ischemia. These findings indicate that alterations in the microcirculation may contribute to functional impairment in PAD patients, which is in agreement with our results.

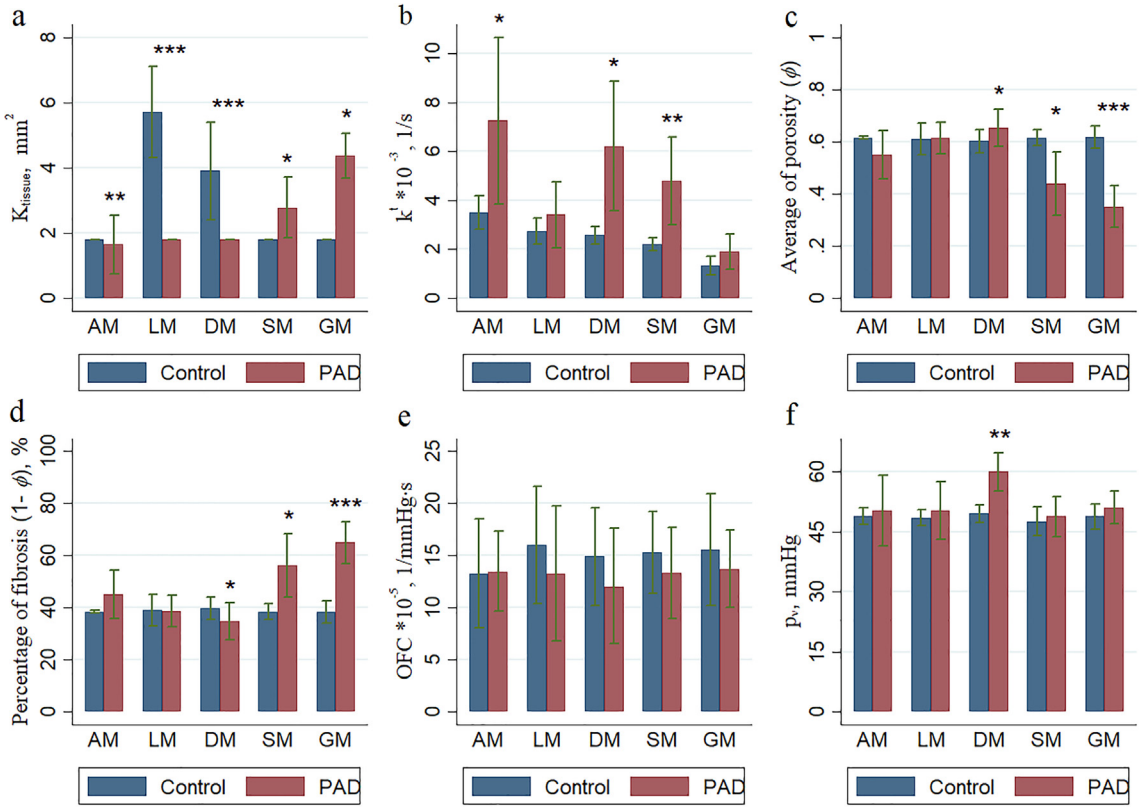

Fig. 6. Plot of (a) intersititial permeability to fluid flow (K_{tissue}), (b) average transfer rate constant (k^t), (c) average of porosity (φ) and (d) percentage of fibrosis (1–φ), (e) outflow filtration coefficient (OFC) and (f) average vascular pressure (p_v) between PAD patients (n = 10) and controls (n = 10) for each muscle region.

Table 6
Correlation analyses for baseline characteristics and modeling parameters.

Variable	Group		Obs	k^t	K_{tissue}	φ	OFC	p_v
Age	Control	r	10	0.52	−0.24	0.36	0.27	0.18
		p-value		0.12	0.51	0.31	0.44	0.62
	PAD	r	10	−0.05	−0.29	−0.26	0.12	−0.08
		p-value		0.89	0.43	0.46	0.74	0.83
	Average	r	20	0.42	0.41	−0.3	0.04	0.24
		p-value		0.06	0.07	0.21	0.86	0.31
Body mass index	Control	r	10	0.06	−0.16	0.03	0.18	−0.03
		p-value		0.86	0.67	0.95	0.62	0.93
	PAD	r	10	−0.14	−0.13	−0.15	0.12	−0.02
		p-value		0.70	0.72	0.68	0.74	0.95
	Average	r	20	0.10	0.17	−0.24	0.09	0.08
		p-value		0.67	0.47	0.30	0.72	0.75
Ankle brachial index (rest)	Control	r	5	0.94	0.86	0.72	0.17	0.26
		p-value		0.017	0.06	0.17	0.78	0.67
	PAD	r	10	−0.05	0.27	0.45	−0.18	−0.01
		p-value		0.88	0.45	0.19	0.61	0.97
	Average	r	15	−0.39	−0.42	0.64	0.04	−0.22
		p-value		0.15	0.12	0.011	0.88	0.42
Ankle brachial index (exercise)	Control	r	5	0.33	−0.28	−0.31	0.82	−0.69
		p-value		0.58	0.64	0.61	0.09	0.19
	PAD	r	7	0.22	0.72	0.57	−0.44	0.15
		p-value		0.63	0.07	0.18	0.32	0.75
	Average	r	12	−0.3	−0.36	0.72	−0.18	−0.28
		p-value		0.34	0.25	0.008	0.57	0.38
Δ of Ankle brachial index	Control	r	5	−0.49	−0.86	−0.77	0.44	−0.69
		p-value		0.40	0.06	0.13	0.46	0.20
	PAD	r	10	0.30	0.29	−0.02	0.08	0.46
		p-value		0.40	0.42	0.95	0.82	0.18
	Average	r	15	−0.04	−0.2	0.20	0.19	0.20
		p-value		0.89	0.48	0.49	0.50	0.48

(*continued on next page*)

Table 6 (*continued*)

Variable	Group		Obs	k^t	K_{tissue}	φ	OFC	p_v
eGFR	Control	r	5	0.13	−0.04	−0.07	0.20	−0.09
		p-value		0.84	0.95	0.91	0.75	0.89
	PAD	r	10	0.33	0.50	0.39	−0.15	0.45
		p-value		0.34	0.14	0.26	0.68	0.19
	Average	r	15	0.24	0.27	0.33	−0.11	0.38
		p-value		0.38	0.33	0.24	0.70	0.17
Hypertension	Control	r	5	−0.89	−0.65	−0.44	−0.35	0.02
		p-value		0.042	0.23	0.46	0.56	0.97
	PAD	r	10	−0.10	0.05	0.05	0.16	−0.02
		p-value		0.79	0.89	0.90	0.65	0.95
	Average	r	15	0.15	0.43	−0.32	−0.08	0.16
		p-value		0.58	0.11	0.25	0.77	0.57

k^t is the transfer rate constant; K_{tissue} is the interstitial permeability; φ is the porosity; OFC is the outflow filtration coefficient; p_v is microvascular pressure.
eGFR: estimated glomerular filtration rate.

The average vascular pressure was higher and *OFC* was lower in PAD patients compared to controls when analyzed over all the muscles regions. Our results indicate that MVP and OFC were heterogeneous across muscle regions, while the CFC was not sensitive with respect to different muscle regions. Bentzer et al. (2001) reported similar findings suggesting that the CFC is independent of perfused capillaries in skeletal muscle of a feline model.

Our work is among the first to report on a computational microvascular model in peripheral artery disease and cardiovascular diseases. This study indicates the potential of numerical CFD simulations which exhibit significant differences between controls and PAD patients and to model blood flow parameters in the leg muscles with different degrees of ischemia and tissue fibrosis.

Limitations: We assumed a finite element model of muscle blood perfusion to describe the exchange between blood plasma and interstitial space. In our simulation, we did not include nonlinear reaction. Blood was assumed as a Newtonian fluid. In addition, physical interactions and leaks between muscle groups were ignored. The proposed micovascular perfusion model could be modified by including interaction terms between the various calf muscle groups. The complexity of muscle blood perfusion was reduced to a selected set of parameters including the geometry of muscle domains, density, dynamic viscosity and tissue porosity, permeability to fluid flow, outflow filtration coefficient, microvascular and osmotic pressure.

5. Conclusions

This study investigated blood perfusion through porous muscles using computational fluid dynamics. The simulation data are in excellent agreement and yield a result with a minimal average deviation from the experimental data, suggesting a reasonable validity and reproducibility of the proposed computational microvascular model in PAD patients and controls. Calf muscle transport properties including k^t, φ, K_{tissue}, p_v and *OFC* exhibit differences between PAD patients and controls.

Funding

We thank all study participants. This work was supported by American Heart Association (AHA) Beginning Grant-in-Aid award (13BGIA16720014, to GB), the Methodist DeBakey Heart Research Award (to DJS), and National Institutes of Health (NIH) awards R01HL137763 (to GB) and K25HL121149 (to GB).

Declaration of Competing Interest

None (OG), none (JS), none (GB), none (DS).

Appendix A

Porous media model

The partial differential equations 1–4 were solved with finite element programming in ANSYS (v.18.2). The full porous model is both a generalization of the Navier-Stokes equations and of Darcy's law commonly used for flows in porous regions. The advection-diffusion equation in a porous medium:

$$\frac{\partial}{\partial t}(\varphi\rho\Phi) + \nabla\cdot(\rho G\cdot U\Phi) - \nabla\cdot(\Gamma G\cdot\nabla\Phi) = \varphi S_t \tag{5}$$

where Γ is the diffusivity, Φ is an additional variable of the conserved quantity per unit volume (non-reacting scalar), $G = \left(G^{ij}\right)$ is the area porosity tensor. In addition to the usual production and dissipation terms, the source term S_t contains transfer terms from the fluid to the solid parts of the porous medium. The equations for conservation of mass and momentum are:

$$\frac{\partial}{\partial t}\varphi\rho + \nabla\cdot(\rho G\cdot U) = 0 \tag{6}$$

and

$$\frac{\partial}{\partial t}(\varphi\rho U) + \nabla\cdot(\rho(G\cdot U)\otimes U) - \nabla \cdot\left(\mu G\cdot\left(\nabla U + (\nabla U)^T - \frac{2}{3}\delta\nabla\cdot U\right)\right) = \varphi S_M - \varphi\nabla p \tag{7}$$

where U is the true velocity, and S_M is a momentum source that includes a contribution $-\zeta\cdot U$ (where $\zeta = \left(\zeta^{ij}\right)$ and represents a resistance to flow in the porous medium).

The momentum loss (applied using Darsy's Law) through an isotropic porous region was formulated using permeability and loss coefficients as follows:

$$S_{M,i} = -\frac{\mu}{K_{tissue}}U_i - K_{loss}\frac{\rho}{2}|U|U_i \tag{8}$$

where K_{tissue} is the permeability and K_{loss} is the quadratic loss coefficient. The linear component of this source represents viscous losses and the quadratic term represents inertial losses. To maintain numerical stability, an artificial diffusion (D_{art}) was added to the diffusive term in Eq. (2) as $D_{art} = (\delta * b * ||U_i||)$, where δ is the tuning parameter, b is element mesh size and U_i is the velocity vector. Relative static pressure was specified over the outlet boundary: $p_{stat,outlet} = 0$.

No-slip boundary condition and the appropriate conditions for velocity components at the wall were used for resolving the con-

fined fluid flow problems on the wall. The velocity of the flow at the wall boundary is set to zero, so the boundary condition for the velocity was set up:

$$U_{wall} = 0$$

The boundary conditions of the model were a set of constraints of the boundary value problems in computational fluid dynamics, and included inlet boundary conditions, outlet boundary conditions, wall boundary conditions. The following boundary conditions are satisfied,

$$-n.(D_i \nabla c_t + U_i c_t) = 0 \quad on \quad \partial\Omega$$

$$-n.U_i = 0 \quad on \quad \partial\Omega$$

U_i is averaged interstitial fluid velocity. Relative static pressure was specified over the outlet boundary and it was equal zero. The velocity of the flow at the wall boundary is set to zero.

Appendix B. Supplementary material

Supplementary data to this article can be found online at https://doi.org/10.1016/j.jbiomech.2019.06.025.

References

Bentzer, P., Kongstad, L., Grande, P.O., 2001. Capillary filtration coefficient is independent of number of perfused capillaries in cat skeletal muscle. Am. J. Physiol. Heart Circ. Physiol. 280, H2697–H2706.

Bonfiglio, A., Leungchavaphongse, K., Repetto, R., Siggers, J.H., 2010. Mathematical modeling of the circulation in the liver lobule. J. Biomech. Eng. 132, 111011.

Bouillard, K., Nordez, A., Hug, F., 2011. Estimation of individual muscle force using elastography. PLoS ONE 6, e29261.

Bouillot, P., Brina, O., Ouared, R., Lovblad, K.O., Farhat, M., Pereira, V.M., 2015. Hemodynamic transition driven by stent porosity in sidewall aneurysms. J. Biomech. 48, 1300–1309.

Boyd, J., Buick, J.M., Green, S., 2007. Analysis of the Casson and Carreau-Yasuda non-Newtonian blood models in steady and oscillatory flows using the lattice boltzmann method. Phys. Fluids 19, 14.

Brunner, G., Bismuth, J., Nambi, V., Ballantyne, C.M., Taylor, A.A., Lumsden, A.B., Morrisett, J.D., Shah, D.J., 2016. Calf muscle perfusion as measured with magnetic resonance imaging to assess peripheral arterial disease. Med. Biol. Eng. Compu. 54, 1667–1681.

Brunner, G., Yang, E.Y., Kumar, A., Sun, W., Virani, S.S., Negi, S.I., Murray, T., Lin, P.H., Hoogeveen, R.C., Chen, C., Dong, J.-F., Kougias, P., Taylor, A., Lumsden, A.B., Nambi, V., Ballantyne, C.M., Morrisett, J.D., 2013. The effect of lipid modification on peripheral artery disease after endovascular intervention trial (ELIMIT). Atherosclerosis 231, 371–377.

Carod-Artal, F.J., Ferreira Coral, L., Stieven Trizotto, D., Menezes Moreira, C., 2009. Self- and proxy-report agreement on the Stroke Impact Scale. Stroke 40, 3308–3314.

Cibis, M., Potters, W.V., Selwaness, M., Gijsen, F.J., Franco, O.H., Arias Lorza, A.M., de Bruijne, M., Hofman, A., van der Lugt, A., Nederveen, A.J., Wentzel, J.J., 2016. Relation between wall shear stress and carotid artery wall thickening MRI versus CFD. J. Biomech. 49, 735–741.

Cohen, J., 1988. Statistical Power Analysis for the behavioral sciences. Lawrence Erlbaum Associates, Hillsdale, NJ.

Criqui, M.H., Aboyans, V., 2015. Epidemiology of peripheral artery disease. Circ. Res. 116, 1509–1526.

Davidson, L.E., Kelley, D.E., Heshka, S., Thornton, J., Pi-Sunyer, F.X., Boxt, L., Balasubramanyam, A., Gallagher, D., M. R. I. A. S. S. o. t. L. A. R. Group, 2014. Skeletal muscle and organ masses differ in overweight adults with type 2 diabetes. J. Appl. Physiol. 1985 (117), 377–382.

Debbaut, C., Monbaliu, D., Casteleyn, C., Cornillie, P., Van Loo, D., Masschaele, B., Pirenne, J., Simoens, P., Van Hoorebeke, L., Segers, P., 2011. From vascular corrosion cast to electrical analog model for the study of human liver hemodynamics and perfusion. IEEE Trans. Biomed. Eng. 58, 25–35.

Debbaut, C., Vierendeels, J., Casteleyn, C., Cornillie, P., Van Loo, D., Simoens, P., Van Hoorebeke, L., Monbaliu, D., Segers, P., 2012. Perfusion characteristics of the human hepatic microcirculation based on three-dimensional reconstructions and computational fluid dynamic analysis. J. Biomech. Eng. 134, 011003.

Dietrich, O., Biffar, A., Baur-Melnyk, A., Reiser, M.F., 2010. Technical aspects of MR diffusion imaging of the body. Eur. J. Radiol. 76, 314–322.

Dubuis, L., Avril, S., Debayle, J., Badel, P., 2012. Identification of the material parameters of soft tissues in the compressed leg. Comput. Methods Biomech. Biomed. Engin. 15, 3–11.

Fowkes, F.G., Rudan, D., Rudan, I., Aboyans, V., Denenberg, J.O., McDermott, M.M., Norman, P.E., Sampson, U.K., Williams, L.J., Mensah, G.A., Criqui, M.H., 2013. Comparison of global estimates of prevalence and risk factors for peripheral artery disease in 2000 and 2010: a systematic review and analysis. Lancet 382, 1329–1340.

Frauziols, F., Rohan, P.Y., Badel, P., Avril, S., Molimard, J., Navarro, L., 2013. Patient-specific modelling of the calf muscle under elastic compression using magnetic resonance imaging and ultrasound elastography. Comput. Methods Biomech. Biomed. Engin. 16 (Suppl 1), 332–333.

Gardner, A.W., Afaq, A., 2008. Management of lower extremity peripheral arterial disease. J. Cardiopulm. Rehabil. Prev. 28, 349–357.

Grishina, O.A., Kirillova, I.V., Glukhova, O.E., 2016. Biomechanical rationale of coronary artery bypass grafting of multivessel disease. Comput. Methods Biomech. Biomed. Engin. 19, 297–305.

Heldin, C.H., Rubin, K., Pietras, K., Ostman, A., 2004. High interstitial fluid pressure - an obstacle in cancer therapy. Nat. Rev. Cancer 4, 806–813.

Hinghofer-Szalkay, H., Greenleaf, J.E., 1987. Continuous monitoring of blood volume changes in humans. J. Appl. Physiol. 1985 (63), 1003–1007.

Holbrook, J., Belousova, T., Short, C.M., Taylor, A.A., Nambi, V., Morrisett, J.D., Ballantyne, C.M., Bismuth, J., Shah, D.J., Brunner, G., 2016. Magnetic resonance imaging based arterial signal enhancement is associated with markers of peripheral artery disease. Circulation 134, A16715.

Hossain, S.S., Zhang, Y., Fu, X., Brunner, G., Singh, J., Hughes, T.J., Shah, D., Decuzzi, P., 2015. Magnetic resonance imaging-based computational modelling of blood flow and nanomedicine deposition in patients with peripheral arterial disease. J. R. Soc. Interface 12.

Javadzadegan, A., Moshfegh, A., Qian, Y., Kritharides, L., Yong, A.S.C., 2019. Myocardial bridging and endothelial dysfunction - Computational fluid dynamics study. J. Biomech. 85, 92–100.

Johnston, B.M., Johnston, P.R., Corney, S., Kilpatrick, D., 2006. Non-Newtonian blood flow in human right coronary arteries: transient simulations. J. Biomech. 39, 1116–1128.

Kamran, H., Nambi, V., Negi, S., Yang, E.Y., Chen, C., Virani, S.S., Kougias, P., Lumsden, A.B., Morrisett, J.D., Ballantyne, C.M., Brunner, G., 2016. Magnetic resonance venous volume measurements in peripheral artery disease (from ELIMIT). Am. J. Cardiol. 118, 1399–1404.

Kenner, T., 1989. The measurement of blood density and its meaning. Basic Res. Cardiol. 84, 111–124.

Kramer, C.M., 2008. Skeletal muscle perfusion in peripheral arterial disease a novel end point for cardiovascular imaging. JACC Cardiovasc. Imaging 1, 351–353.

Leong, H.T., Ng, G.Y., Leung, V.Y., Fu, S.N., 2013. Quantitative estimation of muscle shear elastic modulus of the upper trapezius with supersonic shear imaging during arm positioning. PLoS ONE 8, e67199.

Lim, G.B., 2013. Vascular disease: peripheral artery disease pandemic. Nat. Rev. Cardiol. 10, 552–553.

Maestrini, V., Treibel, T.A., White, S.K., Fontana, M., Moon, J.C., 2014. T1 mapping for characterization of intracellular and extracellular myocardial diseases in heart failure. Curr. Cardiovasc. Imaging Rep. 7, 9287.

MathWorks, T., 2012. MATLAB, and Statistics Toolbox 2012b Natick. Massachusetts, United States.

Newman, A.B., Sutton-Tyrrell, K., Rutan, G.H., Locher, J., Kuller, L.H., 1991. Lower extremity arterial disease in elderly subjects with systolic hypertension. J. Clin. Epidemiol. 44, 15–20.

Phelps, E.A., Garcia, A.J., 2009. Update on therapeutic vascularization strategies. Regen. Med. 4, 65–80.

Pishko, G.L., Astary, G.W., Mareci, T.H., Sarntinoranont, M., 2011. Sensitivity analysis of an image-based solid tumor computational model with heterogeneous vasculature and porosity. Ann. Biomed. Eng. 39, 2360–2373.

Pishko, G.L., Astary, G.W., Zhang, J., Mareci, T.H., Sarntinoranont, M., 2012. Role of convection and diffusion on DCE-MRI parameters in low leakiness KHT sarcomas. Microvasc. Res. 84, 306–313.

Rani, H.P., Sheu, T.W., Chang, T.M., Liang, P.C., 2006. Numerical investigation of non-Newtonian microcirculatory blood flow in hepatic lobule. J. Biomech. 39, 551–563.

Regensteiner, J.G., Wolfel, E.E., Brass, E.P., Carry, M.R., Ringel, S.P., Hargarten, M.E., Stamm, E.R., Hiatt, W.R., 1993. Chronic changes in skeletal muscle histology and function in peripheral arterial disease. Circulation 87, 413–421.

Ren, J., Sherry, A.D., Malloy, C.R., 2015. A simple approach to evaluate the kinetic rate constant for ATP synthesis in resting human skeletal muscle at 7 T. NMR Biomed. 29, 8.

Rippe, B., Townsley, M., Parker, J.C., Taylor, A.E., 1985. Osmotic reflection coefficient for total plasma protein in lung microvessels. J. Appl. Physiol. 1985 (58), 436–442.

Robbins, J.L., Jones, W.S., Duscha, B.D., Allen, J.D., Kraus, W.E., Regensteiner, J.G., Hiatt, W.R., Annex, B.H., 2011. Relationship between leg muscle capillary density and peak hyperemic blood flow with endurance capacity in peripheral artery disease. J. Appl. Physiol. 111, 81–86.

Shrout, P.E., Fleiss, J.L., 1979. Intraclass correlations: uses in assessing rater reliability. Psychol. Bull. 86, 420–428.

Siggers, J.H., Leungchavaphongse, K., Ho, C.H., Repetto, R., 2014. Mathematical model of blood and interstitial flow and lymph production in the liver. Biomech. Model. Mechanobiol. 13, 363–378.

Silva, J.A., White, C.J., Quintana, H., Collins, T.J., Jenkins, J.S., Ramee, S.R., 2004. Percutaneous revascularization of the common femoral artery for limb ischemia. Catheter. Cardiovasc. Interv. 62, 230–233.

Singh, J., Brunner, G., Morrisett, J.D., Ballantyne, C.M., Lumsden, A.B., Shah, D.J., Decuzzi, P., 2018. Patient-specific flow descriptors and normalized wall index in peripheral artery disease: a preliminary study. Comput. Methods Biomech. Biomed. Eng. Imaging Vis. 6, 119–127.

Smye, S.W., Evans, C.J., Robinson, M.P., Sleeman, B.D., 2007. Modelling the electrical properties of tissue as a porous medium. Phys. Med. Biol. 52, 7007–7022.
Stoner, M., Defreitas, D., Manwaring, M., et al., 2008. Cost per day of patency: understanding the impact of patency and reintervention in a sustainable model of healthcare. *J. Vasc. Surg.* 48 (6), 1489–1496.
Stylianopoulos, T., Jain, R.K., 2013. Combining two strategies to improve perfusion and drug delivery in solid tumors. Proc. Natl. Acad. Sci. USA 110, 18632–18637.
Thompson, R.B., Aviles, R.J., Faranesh, A.Z., Raman, V.K., Wright, V., Balaban, R.S., McVeigh, E.R., Lederman, R.J., 2005. Measurement of skeletal muscle perfusion during postischemic reactive hyperemia using contrast-enhanced MRI with a step-input function. Magn. Reson. Med. 54, 289–298.
Tofts, P.S., Kermode, A.G., 1991. Measurement of the blood-brain barrier permeability and leakage space using dynamic MR imaging. 1. Fundamental concepts. Magn. Reson. Med. 17, 357–367.
van der Plaats, A., Hart, N.A.t, Verkerke, G.J., Leuvenink, H.G., Verdonck, P., Ploeg, R.J., Rakhorst, G., 2004. Numerical simulation of the hepatic circulation. *Int. J. Artif. Organs.* 27, 222–230.
Vankan, W.J., Huyghe, J.M., van Donkelaar, C.C., Drost, M.R., Janssen, J.D., Huson, A., 1998. Mechanical blood-tissue interaction in contracting muscles: a model study. J. Biomech. 31, 401–409.
Wu, W.C., Wang, J., Detre, J.A., Wehrli, F.W., Mohler 3rd, E., Ratcliffe, S.J., Floyd, T.F., 2008. Hyperemic flow heterogeneity within the calf, foot, and forearm measured with continuous arterial spin labeling MRI. Am. J. Physiol. Heart Circ. Physiol. 294, H2129–H2136.
Yang, E.Y., Brunner, G., Dokainish, H., Hartley, C.J., Taffet, G., Lakkis, N., Taylor, A.A., Misra, A., McCulloch, M.L., Morrisett, J.D., Virani, S.S., Ballantyne, C.M., Nagueh, S.F., Nambi, V., 2013. Application of speckle-tracking in the evaluation of carotid artery function in subjects with hypertension and diabetes. J. Am. Soc. Echocardiogr. 26, (901–909) e1.
Zhang, P., Liu, X., Sun, A., Fan, Y., Deng, X., 2015. Hemodynamic insight into overlapping bare-metal stents strategy in the treatment of aortic aneurysm. J. Biomech. 48, 2041–2046.
Zhao, F., van Rietbergen, B., Ito, K., Hofmann, S., 2018. Flow rates in perfusion bioreactors to maximise mineralisation in bone tissue engineering in vitro. J. Biomech. 79, 232–237.